Physics of Plasmas

RESEARCH ARTICLE | OCTOBER 10 2025

Determining the nanostructure of polymer foams using 3D ptycho-tomography for inertial fusion energy applications

Special Collection: Progress in Inertial Fusion Energy Research: Two Years After Ignition

L. Hancock ; K. Mertes ; A. Carr ; X. Xia ; C. Sweeney ; M. Ikeya ; Y. Chen; V. Esposito; D. Hodge ; O. Hoidn; W. M. Martin ; M. Mettry-Yassa ; C. Parisuaña; T. Sato ; Y. Sechrest ; M. H. Seaberg ; S. Song ; A. Vong; A. White; R. L. Sandberg ; A. E. Gleason

Check for updates

Phys. Plasmas 32, 102707 (2025)
https://doi.org/10.1063/5.0272192
CHORUS

View Online
Export Citation

Articles You May Be Interested In

Recent advances in small angle x-ray scattering for superlattice study

Appl. Phys. Rev. (January 2021)

X-ray ptychography on low-dimensional hard-condensed matter materials

Appl. Phys. Rev. (March 2019)

Optics for broadband x-ray ptychography

Rev. Sci. Instrum. (August 2025)

14 October 2025 21:21:13

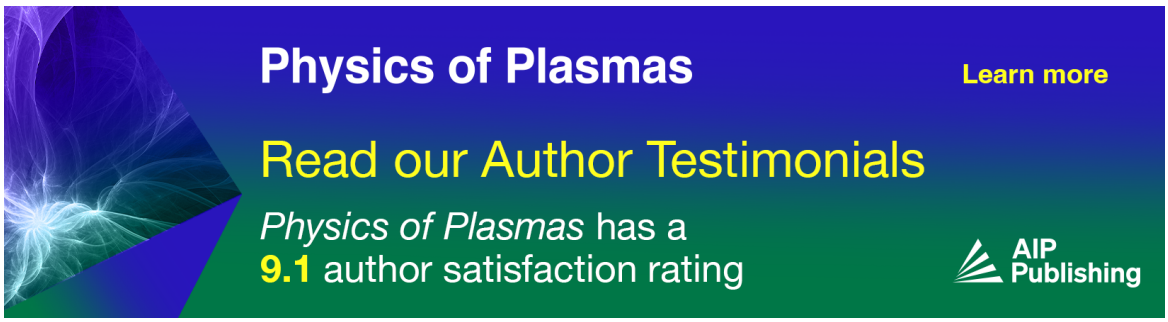

AIP Publishing

Physics of Plasmas ARTICLE pubs.aip.org/aip/pop

Determining the nanostructure of polymer foams using 3D ptycho-tomography for inertial fusion energy applications

Cite as: Phys. Plasmas **32**, 102707 (2025); doi: 10.1063/5.0272192
Submitted: 22 March 2025 · Accepted: 28 September 2025 ·
Published Online: 10 October 2025

View Online Export Citation CrossMark

L. Hancock,[1,2,a)] K. Mertes,[3] A. Carr,[3] X. Xia,[4] C. Sweeney,[3] M. Ikeya,[1,5] Y. Chen,[5] V. Esposito,[5] D. Hodge,[1,2] O. Hoidn,[5] W. M. Martin,[1,5,6] M. Mettry-Yassa,[4] C. Parisuaña,[1,5,7] T. Sato,[5] Y. Sechrest,[3] M. H. Seaberg,[5] S. Song,[5] A. Vong,[8] A. White,[5] R. L. Sandberg,[1,2] and A. E. Gleason[1,5]

AFFILIATIONS

[1]DOE IFE-STAR RISE-hub, Colorado State University (CSU), Fort Collins, Colorado 80523, USA
[2]Physics Department, Brigham Young University, Provo, Utah 84602, USA
[3]Los Alamos National Laboratory, Los Alamos, New Mexico 87545, USA
[4]Lawrence Livermore National Laboratory, Livermore, California 94550, USA
[5]SLAC National Accelerator Laboratory, Menlo Park, California 94025, USA
[6]Physics Department, Stanford University, Stanford, California 94305, USA
[7]Department of Mechanical Engineering, Stanford University, Stanford, California 94305, USA
[8]Argonne National Laboratory, Lemont, Illinois 60439, USA

Note: This paper is part of the Special Topic on Progress in Inertial Fusion Energy Research: Two Years After Ignition.
[a)]**Author to whom correspondence should be addressed:** levijh1@gmail.com

14 October 2025 21:21:13

ABSTRACT

Polymer foams play a critical role in contemporary inertial fusion energy (IFE) target designs by enhancing energy yield and optimizing implosion dynamics. However, the lack of high-resolution characterization of the nanostructure of these foams restricts progress in fusion science. In this work, we demonstrate the first high-resolution three-dimensional (3D) reconstruction of a low-density, Si-doped polymer foam fabricated via two-photon polymerization, using ptychographic x-ray computed tomography (PXCT) at an x-ray free electron laser (XFEL). This imaging method reconstructs two-dimensional (2D) attenuation and phase information at multiple sample angles that are combined into a 3D density map used to extract local mass density and determine structural dimensions. We achieve a 2D spatial resolution of 19 ± 3 nm on a high-contrast Ronchi pattern target and 78.7 ± 3 nm for low-contrast polymer foams, marking a significant advancement for XFEL-based ptychography of low-density materials. Furthermore, our experimental results reveal an average foam strut thickness of $1.17 \pm 0.4\ \mu$m, consistent with fabrication expectations, and a reconstructed average mass density of 0.35 g/cc, aligning closely with the predicted density of 0.29 g/cc. These findings provide important insights for improving foam design and refining radiation hydrodynamics modeling in future IFE experiments. Our study establishes PXCT at an XFEL as a powerful tool for high-resolution characterization of fusion-relevant materials, paving the way for enhanced target performance in IFE research.

© 2025 Author(s). All article content, except where otherwise noted, is licensed under a Creative Commons Attribution (CC BY) license (https://creativecommons.org/licenses/by/4.0/). https://doi.org/10.1063/5.0272192

I. INTRODUCTION

Recent advancements in inertial fusion energy (IFE)[1] research aim to bring fusion power closer to commercial viability.[2–6] Many designs for achieving high energy gain require precise control over target implosions,[7,8] which depend on complex material interactions and hydrodynamics. One approach under investigation involves incorporating polymer foams into fusion targets.[9–11] These foams enable higher burn-up fractions and gains, improve control over implosion dynamics, and simplify target fabrication.[12–14] Tailoring the structure of the polymer foams is also important for plasma dynamics during the implosion process, linking material design directly to fusion performance.[13]

© Author(s) 2025

Radiation hydrodynamics modeling is crucial for optimizing these targets, but its accuracy depends on a detailed characterization of the foam's micro- and nanoscale structure. High-resolution imaging techniques provide essential input for refining these models. Here, we characterize a Si-doped polymer foam pillar ($C_{48}H_{72}Si_8O_{28}$) fabricated using two-photon polymerization[15–17] at the Lawrence Livermore National Laboratory, to improve understanding of its structural properties.

We image the foam using ptychographic x-ray computed tomography (PXCT),[18–20] a lensless coherent x-ray imaging technique that reconstructs a high-resolution three-dimensional (3D) volume from two-dimensional (2D) ptychographic projections.[21] As an x-ray diffraction imaging method, PXCT recovers both amplitude and phase information, enabling quantitative mass density analysis and high-resolution imaging of weakly absorbing materials like polymer foams. While PXCT has been demonstrated at synchrotrons,[19] x-ray free-electron lasers (XFELs) offer advantages such as higher brilliance and coherence, improving resolution and data acquisition speed. This experiment presents one of the first instances of PXCT performed at an XFEL.[22,23]

Using the Linac Coherent Light Source (LCLS) at the SLAC National Accelerator Laboratory, we generate a high-resolution 3D image of a Si-doped foam pillar. We report localized mass density and wall thickness measurements to refine and improve future radiation hydrodynamics modeling and demonstrate a robust 3D visualization approach for low-density materials.

II. METHODS

In this section, we describe the PXCT method at the LCLS. We describe the experimental setup, reconstruction of the 2D projections and 3D volume, and how we subsequently extract the mass density from the 3D volume.

A. Experimental setup

Ptychotomography of the foam samples was conducted at the x-ray pump probe (XPP) instrument at the Linac Coherent Light Source (LCLS). As shown in Fig. 1, our experimental setup closely follows the designs used by Carr *et al.*[22] and Pound *et al.*[23] Coherent, ultrafast pulses of 8.87 keV x-rays at 120 Hz were passed through a silicon monochromator and then focused onto the sample with a Fresnel zone plate with a focal length of 53.2 mm and an aperture of 150 μm. An order sorting aperture was placed 6 mm upstream of the focus (47.2 mm downstream of the lens). The sample was then placed 1.22 mm downstream of the focus to provide a spot size of approximately 3 μm full width at half maximum (FWHM). The sample was rastered through the spot with 90% overlap through over 1000 positions and then rotated after each tomography scan. A JungFrau 1M detector was placed 3.2 m behind the sample.[24] An evacuated flight tube with Kapton windows was placed between the sample and the detector to minimize air scattering losses.

B. 2D projections

Ptychography is a coherent diffractive imaging technique that reconstructs high-resolution images by analyzing overlapping diffraction patterns from scanned illumination spots. We use ptychography because of its unique ability to recover both the amplitude and the phase of scattered x-rays, providing information on both x-ray attenuation and phase shifts induced by the sample. For low-contrast materials with minimal x-ray absorption, phase contrast often provides more valuable information,[25] as it offers higher sensitivity and can be correlated with the material's mass density. Polymer foams, due to their low density, exhibit weak x-ray attenuation and minimal phase contrast, presenting significant challenges for high-resolution imaging and characterization.

To monitor the sample position and detect potential anomalies during scanning, 2D ptychography images were reconstructed in real-time using the GPU-accelerated KMPty software.[22,26] Early reconstructions of the polymer foam pillar confirmed the anticipated weak x-ray attenuation and minimal phase contrast, highlighting the need for contrast enhancement.

Prior to experimentation, we included silicon in the polymer stoichiometry to enhance x-ray scattering and improve image contrast. During the experiment, we further increased the average atomic number of the foam sample to increase x-ray scattering by briefly soaking the foam pillars in a colloidal gold solution. We applied the colloidal gold coating by depositing a droplet onto the pillar, allowing the foam to absorb it for one second. Excess residual liquid was removed.

C. 3D reconstruction

To collect the images required for a 3D tomographic reconstruction of the foam pillar, we recorded 800 ptychography scans with a

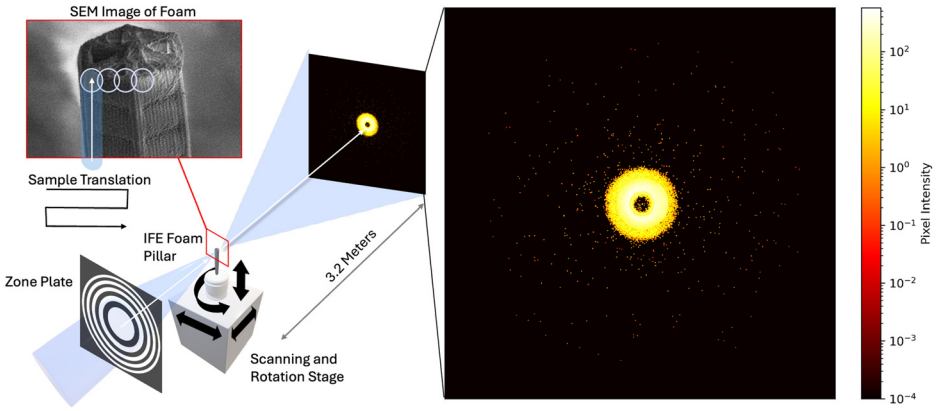

FIG. 1. Schematic of ptycho-tomography experiment. A zone plate focuses the XFEL beam onto a foam pillar sample. The sample is rastered and rotated through the beam. A detector located 3.2 m away collects far-field diffraction patterns of scattered x-rays. The diffraction pattern shown (right) displays photon counts per pixel from a single exposure collected from one position of a 2D raster scan.

14 October 2025 21:21:13

© Author(s) 2025

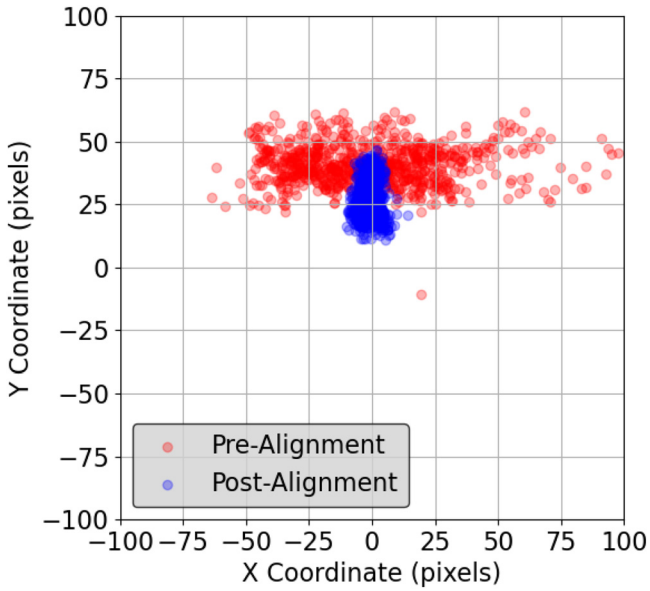

FIG. 2. The plotted 2D ptychography centroids of each of the 800 projections used to create the 3D tomography scan. The image demonstrates how the overall alignment improves as a result of the image registration procedure.

0.45° step size over a full 360° rotation. However, a key challenge in the reconstruction process was accurately aligning the 2D ptychography projections after they were measured and reconstructed. Data collection occurred over two days, during which the sample was periodically repositioned on the beamline, leading to shifts in the 2D reconstructions. To achieve a high-resolution 3D reconstruction, each 2D image must be precisely aligned along the same axis of rotation;[27] otherwise, misalignment introduces blurring and artifacts into the final 3D reconstruction. Previous tomography studies outline several alignment strategies, including the joint iterative re-projection,[28] vertical mass fluctuation,[29] and optical flow[30] algorithms. Each of these algorithms was tested, but due to the low-contrast nature of the projections, significant noise, and lack of sharp features to align to, these algorithms were largely unsuccessful.

We applied the following sequence of alignment strategies in the given order:

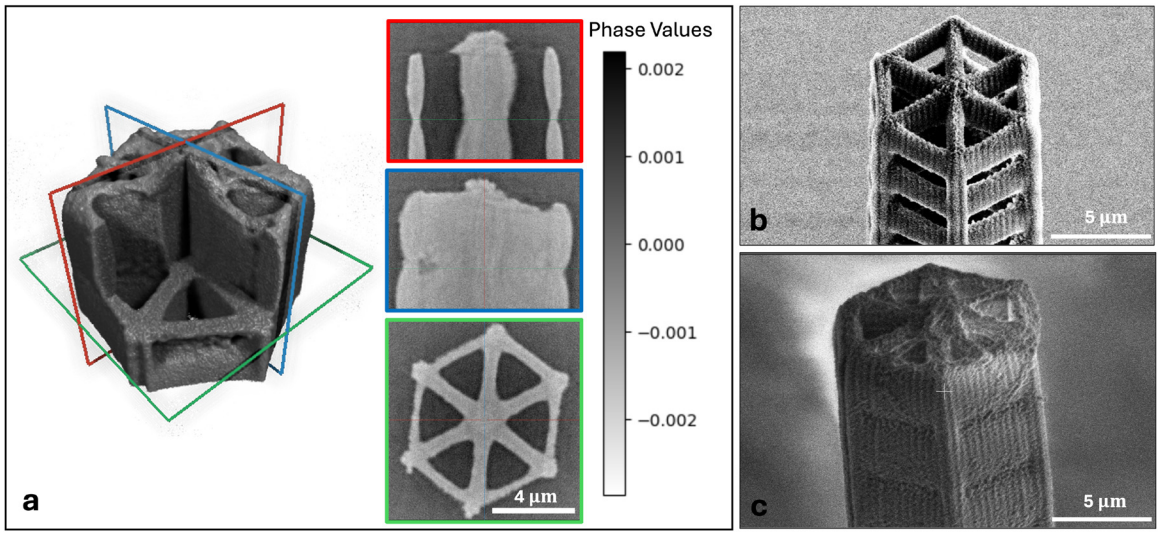

FIG. 3. Slices through a 3D reconstructed volume and SEM images of a polymer foam pillar before and after a colloidal gold solution soak. (a) The reconstructed volume with a cubic cutout (left) and three orthogonal slices (right) to show the internal structure of the foam pillar. (b) SEM image of a similar Si-doped foam pillar before imaging. (c) SEM image of the foam pillar after soaking in a colloidal gold solution, which caused the empty space between struts to fill in.

14 October 2025 21:21:13

© Author(s) 2025

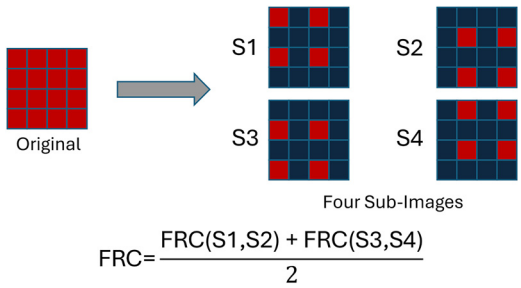

FIG. 4. Illustration of the single-image FRC technique. We split the image into four sub-images. Then we performed an FRC calculation on two pairs of sub-images, which are averaged to calculate an overall FRC curve.

1. **Manual shift alignment**—each projection was manually adjusted in the Fiji[31] image processing software by visually shifting the image such that the tip of the sample pillar was centered horizontally and aligned to a consistent vertical height across all projections.
2. **Cross-correlation shift (2 iterations)**—each projection was aligned by shifting it according to the peak value of its cross-correlation with the adjacent recorded projection, which was taken at the same position but rotated by 0.45°.
3. **Horizontal center-of-mass centering**[32]—implemented using the Tomopy Python library.[33]
4. **Projection matching alignment (3 iterations)**[29]—using a reference reconstructed volume from the previously aligned projection, each measured projection was aligned to its corresponding simulated projection (forward projection of the volume at the same angle) by shifting it to the position corresponding to the maximum cross-correlation value.
5. **Horizontal center-of-mass centering**[32]—reapplied using TomoPy[33] to correct for any accumulated drift introduced during projection matching.

As a result, the 3D tomography algorithm was successfully reconstructed with high resolution, enabling the analysis presented in Sec. III. The improvement in alignment following this procedure is shown in Fig. 2.

After alignment, we evaluated over 15 tomography algorithms from the Tomopy Python library, using GPU-accelerated algorithms from the Astra[33,34] extension toolbox. The simultaneous iterative reconstruction technique (SIRT) produced the best high-resolution 3D reconstruction for this dataset. Although the supervoxel model-based iterative reconstruction (SVMBIR)[35] python package's implementation of the MBIR algorithm produced similarly high-resolution results, SIRT was preferred due to its ability to generate a 3D reconstruction approximately 18 times faster than the MBIR implementation.

D. Mass density calculation

We calculated the mass density distribution by using phase shift information to estimate localized mass density.[22,36] Each voxel, or 3D pixel, in the ptycho-tomography reconstruction corresponds to a phase shift of diffracted x-rays caused by material density at the voxel location. These phase shifts are proportional to localized electron density, which we then converted to a mass density based on the material's assumed chemical composition. Appendix provides more details of the process.

III. RESULTS

In Sec. III, we present our imaging results, including analysis of resolution from a high contrast test object and the IFE foam. We also present the retrieved IFE pillar morphology and mass densities.

A. Imaging resolution

Before producing the 3D volume reconstruction, we expected the reconstructed foam pillar to resemble the structure shown in the scanning electron microscopy image in Fig. 3(b), with a repeated lattice of 1.1 μm diameter bars connecting supporting struts. However, analysis of the reconstructed 3D volume revealed changes in the pillar's geometry, likely caused by the colloidal gold solution used in an attempt to improve the convergence of the ptychography reconstruction process. It appears that the solution caused the space between the struts in the outer wall to fill in. The alteration in the pillar's shape was confirmed with scanning electron microscopy, as shown in Fig. 3(c).

Resolution was evaluated using a single image Fourier ring correlation (FRC) technique[37,38] with a half-bit threshold.[39] This method partitions the reconstructed 2D image by assigning every other pixel to one of four subimages (see Fig. 4). We compare the Fourier transforms of two subimages to assess frequency-dependent correlation, which corresponds to concentric rings in Fourier space. We then average the results from two different FRC calculations to calculate an overall FRC correlation curve for the single image. The resolution is defined as the spatial frequency at which the correlation curve falls below the half-bit threshold [see Fig. 5(b)].

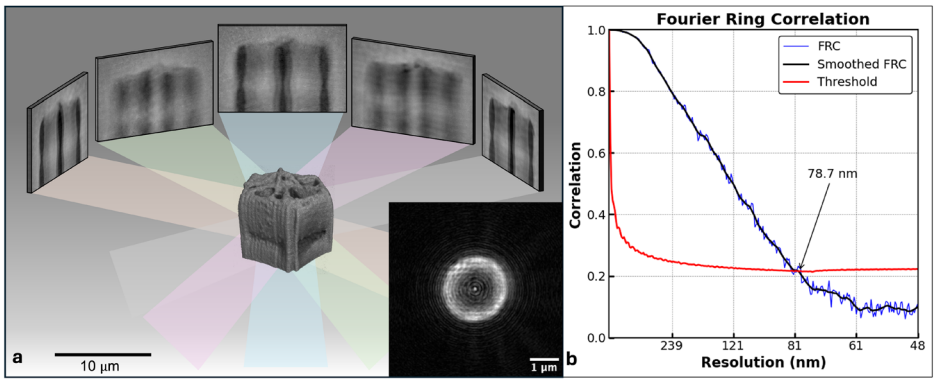

FIG. 5. Projections through a reconstructed volume and resolution measurement. (a) Many 2D projections combine to form a 3D reconstructed volume. A reconstructed probe is produced for each scan. An example reconstructed probe is shown (inset). (b) Fourier ring correlation (FRC) imaging demonstrates a 78.7 nm resolution using a half-bit threshold (see Sec. III A and Fig. 4 for explanation of method).

14 October 2025 21:21:13

© Author(s) 2025

To assess the resolution of our method, several scans were taken of a high-contrast (e.g., 150 nm Pt on a SiN substrate) Ronchi pattern target (see Fig. 6). Using this technique, the high-contrast target reconstruction produced a resolution of 19 ± 3 nm. This is a high spatial resolution record achievement for XFEL-based ptychography measurements to date. Resolution measurements on a low-contrast projection through the Si-doped polymer foam pillar produced a resolution of 78.7 ± 3 nm. We found that the FRC-based resolution was both sample-dependent, with higher-contrast objects yielding better spatial resolution, and scan-dependent, due to beam jitter in the focusing optic.

B. Pillar dimensions and mass density

A 3D thickness mesh of the foam pillar, generated using the Dragonfly 3D World software 2024.1 (Comet Technologies Canada Inc., Montreal, QC, Canada), displays the pillar's thickness at each point in the volume (see Fig. 7). The thickness mesh displays a color-coded 3D map representing the local thickness of the foam pillar by calculating the shortest distance between opposing surfaces within a volume. The Si-doped polymer foam after the colloidal gold solution soak exhibits slight shape variations, making direct comparison challenging. Nevertheless, the mass density distribution shows an average thickness of 1.17 ± 0.4 μm, which is consistent with the expected fabrication value of 1.1 μm from a scanning electron microscope image.

This study also aimed to compare the expected and measured mass density of the Si-doped foam pillar based on 3D volume reconstruction. The expected density was estimated based on the fabrication materials and processes. The photo-crosslinked Si-doped polymer has a solid density of 1.2 g/cc. The 3D printed foam has a lattice geometry that occupies 30% of a cylindrical volume with a 6 μm base radius. By adding porogen into the 3D printing resin formulation that does not participate in the polymerization reaction, the printed struts have an estimated porosity of 20%. These parameters yield a predicted average mass density of approximately 0.29 g/cc within the 6 μm radius cylindrical region enclosing the pillar.

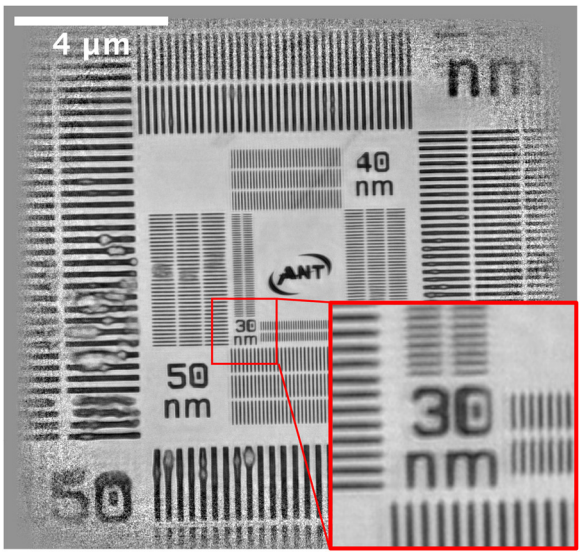

FIG. 6. 2D ptychography reconstruction of a high-contrast Ronchi ruling target. This reconstructed phase image demonstrates the capability of high-resolution ptychography at the LCLS to achieve 19 nm resolution.

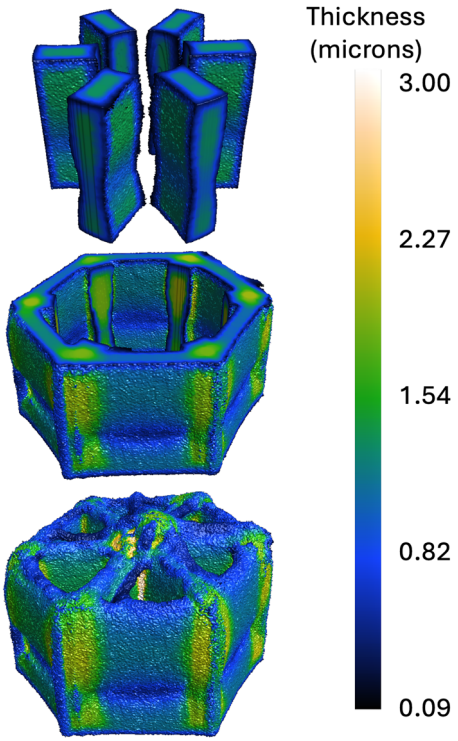

FIG. 7. Wall thickness measurements of various regions of a Si-doped polymer foam pillar. We show thickness (in micrometers) for the entire pillar (bottom), the outer wall (middle), and the interior struts (top). Thickness is measured as the shortest distance between opposing surfaces within a volume.

We show the mass density distribution from the reconstructed volume in Fig. 8 as a normalized relative frequency distribution of voxel values corresponding to the mass density at each voxel in a cylindrical region within the 6 μm radius cylindrical region enclosing the pillar. The distribution demonstrates an average material mass density around 0.68 g/cc, but when averaged over the entire cylindrical volume, we calculate an average density of 0.35 g/cc. We believe that the observed deviation of 0.35 g/cc from the estimated 0.29 g/cc may arise from one or more factors: the colloidal gold solution treatment used to enhance x-ray contrast, genuine density variation within the sample, or artifacts introduced by averaging the mass density over a limited axial length of the foam pillar. The imaged volume spans approximately one unit cell in the z-direction, so cropping effects could contribute significantly to the measured density.

IV. DISCUSSION/CONCLUSION

This work demonstrates that the PXCT is a viable method for 3D characterization of polymer foams used in fusion targets. Our approach produced a 3D reconstruction of a Si-doped polymer foam pillar, structurally consistent with expectations from SEM imaging and the two-photon polymerization process used in fabrication.

14 October 2025 21:21:13

© Author(s) 2025

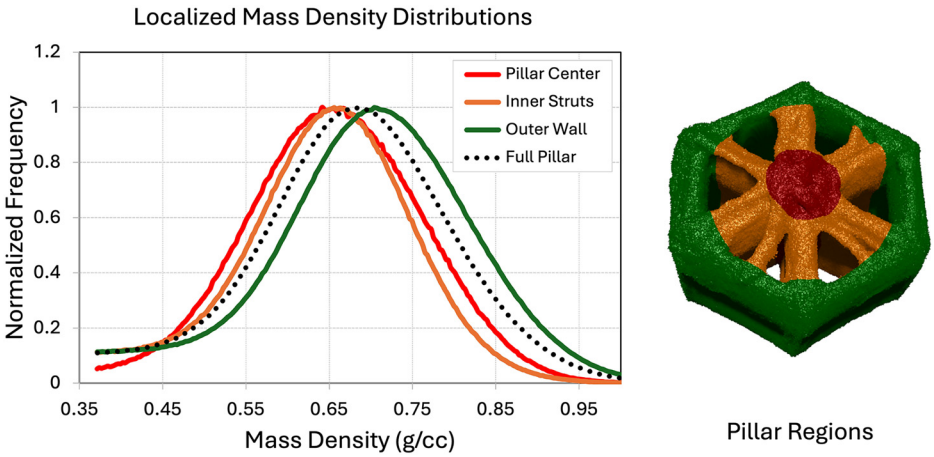

FIG. 8. Normalized mass density distributions for various regions of a Si-doped polymer foam pillar. Mass density is calculated in each voxel and assigned to a region of the foam, shown by different colors. The distributions are normalized to a maximum frequency value of 1. The reconstructed pillar (right) illustrates the regions referenced in the mass distribution plot (left).

Additionally, we validated ptycho-tomography as a viable method for measuring localized mass density within a volume.

We demonstrated that ptycho-tomography effectively overcomes the inherent challenges of visualizing the micro- to nano-structure of low-density polymer foams. The low-density foam pillar scatters very few photons (see Fig. 1); however, those scattered photons encode sufficient information to reconstruct high-quality 2D projections, enabling accurate 3D reconstruction. Moreover, our results corroborate the findings of previous experimentation regarding the advantages of ptycho-tomography at an XFEL.[22]

Ptycho-tomography at XFELs could be upscaled in its ability to analyze the nanostructure of materials in real-time. The high repetition rate, brilliance and coherence of XFELs enable rapid, scalable characterization. Future laser- or pulsed power-based IFE power plants will require high-throughput analysis of fusion capsules to sustain ignition and burn. A new paradigm for establishing the viability and verification for batches of capsules will be required for any rep-rated IFE concept. This means innovating methods for marking initial capsule viability, tracking motion and engagement with the driver are required. As part of the suite of new diagnostics that could aid in this effort, advances in computational power and methods such as single-shot x-ray ptychography[40] could be beneficial. High-throughput x-ray and optical diagnostics will be critical to IFE power plant operations. Novel x-ray techniques, such as the ptycho-tomography measurements described here, are valuable, not only for the characterization of foam micro- and nanostructures, density, and chemistry requisite in radiation hydrocode models, but also in showcasing how 3D visualization at the nanoscale can be accelerated, supporting the rapid characterization necessary for IFE applications.

ACKNOWLEDGMENTS

The authors, L.H., R.S., D.H., W.M., C.P., and A.G., are grateful for funding from the Office of Science, Fusion Energy Sciences, under Award No. DE-SC 0024882: IFE-STAR issued as SLAC FWP 101126 through the IFE RISE Hub partnership. Use of the Linac Coherent Light Source (LCLS), the SLAC National Accelerator Laboratory, is supported by the U.S. Department of Energy, Office of Science, Office of Basic Energy Sciences under Contract No. DE-AC0276SF00515. Part of this work was performed at the Stanford Nano Shared Facilities (SNSF), supported by the National Science Foundation under award ECCS-2026822. L.H. acknowledges support from BYU CMPS College Experiential Learning Funds. W.M. acknowledges support from the National Science Foundation Graduate Research Fellowship Program under Grant No. DGE-2146755. X. X. and M. M. acknowledge support by the Lawrence Livermore National Laboratory's Lab Directed Research and Development Program (23-ERD-027). Work at LLNL was performed under the auspices of the U.S. Department of Energy by the Lawrence Livermore National Laboratory under Contract DE-AC52-07NA27344. A.V. acknowledges support from the U.S. Department of Energy (DOE) Office of Science-Basic Energy Sciences award Collaborative Machine Learning Platform for Scientific Discovery 2.0. This research used resources of the Advanced Photon Source, a U.S. Department of Energy (DOE) Office of Science User Facility operated for the DOE Office of Science by the Argonne National Laboratory under Contract No. DE-AC02-06CH11357.

AUTHOR DECLARATIONS

Conflict of Interest

The authors have no conflicts to disclose.

Author Contributions

L. Hancock: Data curation (equal); Formal analysis (equal); Investigation (equal); Methodology (equal); Project administration (equal); Software (equal); Validation (equal); Visualization (equal); Writing – original draft (equal); Writing – review & editing (equal). **K. Mertes:** Conceptualization (equal); Data curation (equal); Formal analysis (equal); Investigation (equal); Methodology (equal); Software (equal); Supervision (supporting); Validation (equal); Visualization (equal); Writing – review & editing (supporting). **A. Carr:** Conceptualization (equal); Data curation (equal); Formal analysis (equal); Methodology (equal); Software (equal); Supervision (equal); Validation (equal); Writing – review & editing (supporting). **X. Xia:** Conceptualization (equal); Formal analysis (equal); Investigation (equal); Methodology (equal); Resources (equal); Validation (equal); Visualization (equal); Writing – review & editing (equal). **C. Sweeney:**

14 October 2025 21:21:13

© Author(s) 2025

Data curation (equal); Formal analysis (equal); Investigation (equal); Methodology (equal); Software (equal); Supervision (supporting); Visualization (equal); Writing – review & editing (equal). **M. Ikeya:** Data curation (equal); Formal analysis (equal); Investigation (equal); Methodology (equal); Visualization (equal). **Y. Chen:** Investigation (supporting); Resources (equal); Visualization (equal). **V. Esposito:** Formal analysis (supporting); Resources (equal); Software (equal); Visualization (equal). **D. Hodge:** Data curation (equal); Formal analysis (supporting); Investigation (equal); Methodology (equal); Supervision (supporting); Validation (supporting); Visualization (supporting); Writing – review & editing (equal). **O. Hoidn:** Investigation (equal); Resources (equal); Visualization (equal). **W. M. Martin:** Formal analysis (equal); Investigation (equal); Methodology (equal); Validation (equal); Writing – original draft (supporting); Writing – review & editing (equal). **M. Mettry-Yassa:** Resources (equal); Validation (equal). **C. Parisuaña:** Investigation (supporting); Methodology (equal). **T. Sato:** Data curation (equal); Investigation (equal); Methodology (equal); Resources (equal); Software (equal). **Y. Sechrest:** Formal analysis (supporting); Methodology (equal); Supervision (equal); Validation (supporting). **M. H. Seaberg:** Data curation (equal); Formal analysis (equal); Investigation (equal); Methodology (equal); Resources (equal); Software (supporting); Visualization (equal). **S. Song:** Investigation (equal); Methodology (equal); Resources (equal); Software (supporting); Visualization (supporting). **A. Vong:** Formal analysis (supporting); Methodology (equal); Software (supporting). **A. White:** Investigation (supporting); Resources (equal). **R. L. Sandberg:** Conceptualization (equal); Data curation (equal); Formal analysis (equal); Funding acquisition (equal); Investigation (equal); Methodology (equal); Project administration (equal); Supervision (equal); Validation (equal); Writing – original draft (equal); Writing – review & editing (equal). **A. E. Gleason:** Conceptualization (lead); Data curation (equal); Formal analysis (equal); Funding acquisition (lead); Investigation (lead); Methodology (lead); Project administration (lead); Resources (equal); Supervision (lead); Validation (equal); Writing – original draft (supporting); Writing – review & editing (equal).

DATA AVAILABILITY

The data that support the findings of this study are available from the corresponding author upon reasonable request.

APPENDIX: MASS DENSITY AND CHEMICAL COMPOSITION TESTS

Phase shift information can be reconstructed from recorded diffraction patterns using ptychography. Phase shifts arise as x-rays propagate through a finite-density material, leading to a 2D projection of the phase as given by[25,36]

$$\phi = -k \int \delta(x, y, z) dz, \tag{A1}$$

where k represents the wave number and $\delta(x, y, z)$ represents the real part of the index of refraction ($n = 1 - \delta + i\beta$) as a function of wavelength and spatial coordinates x, y, and z. The integration along z accounts for the total phase shift due to the material's varying density in the direction of x-ray propagation. Relative to vacuum, this results in the phase advancing when encountering denser material,[41] with higher negativity corresponding to greater material density.

The reconstructed 3D phase volume provides a voxel mapping of phase reduction due to the material's electron density. The total projected electron density, σ_e, relates to the reconstructed phase difference by[22]

$$\sigma_e = -\frac{\phi}{\lambda r_0}, \tag{A2}$$

where λ is the x-ray wavelength and r_0 is the classical electron radius. This equation is only valid away from absorption edges, a condition that is satisfied in this experiment. This electron density can be scaled over the 23.29 nm voxel size to determine the electron density with units of n_e/m^3 at each voxel.

The mass density relates to the electron density by[22]

$$\sigma_m = \frac{A}{Z} u \sigma_e, \tag{A3}$$

where A is the mass number of the molecule, Z is the number of electrons in a stable molecule of the sample's assumed chemical composition, and u is the atomic mass unit. The resultant mass density is in units g/cc. The assumed chemical composition corresponds to the Si-doped polymer foam porogen used to fabricate the pillar: $C_{48}H_{72}Si_8O_{28}$.

Following a colloidal gold soak applied to the polymer foam pillar to enhance x-ray scattering and improve ptychography convergence, the chemical composition at each voxel changed slightly.

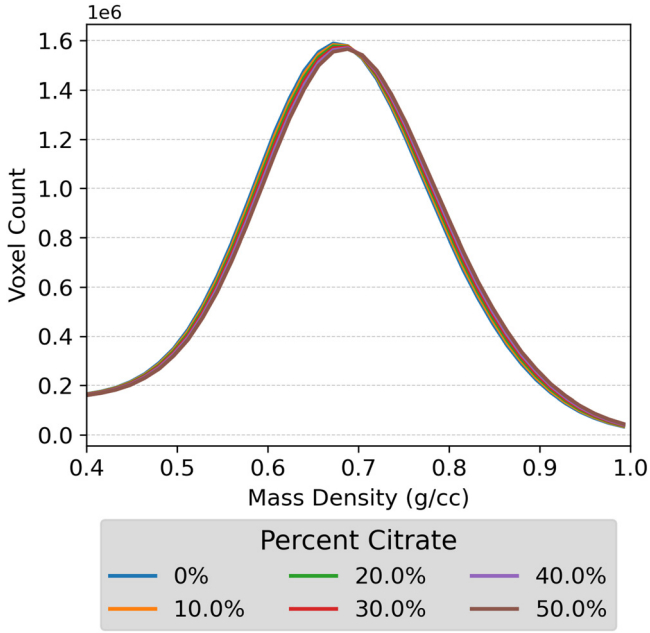

FIG. 9. Comparison of mass density distributions with varying percentages of citrate. In the conversion from electron density to mass density [see Eq. (A3)], the varying percentages of citrate influence the ratio of electrons to molecular mass but produce a negligible effect on mass density.

14 October 2025 21:21:13

© Author(s) 2025

The colloidal gold solution consists primarily of citrate ($C_6H_5O_7$), so we tested the impact of different absorption percentages. Across a range of 0%–50% citrate absorption, the change in mass density was negligible, as seen in Fig. 9. Thus, we concluded that we can assume a uniform composition at each voxel for accurate localized mass density calculations.

REFERENCES

[1]R. Betti and O. A. Hurricane, "Inertial-confinement fusion with lasers," Nat. Phys. **12**(5), 435–448 (2016).

[2]H. Abu-Shawareb *et al.*, "Lawson criterion for ignition exceeded in an inertial fusion experiment," Phys. Rev. Lett. **129**, 075001 (2022).

[3]A. Pak, A. B. Zylstra, K. L. Baker, D. T. Casey, E. Dewald, L. Divol, M. Hohenberger, A. S. Moore, J. E. Ralph, D. J. Schlossberg, R. Tommasini, N. Aybar, B. Bachmann, R. M. Bionta, D. Fittinghoff, M. G. Johnson, H. G. Kleinrath, V. G. Kleinrath, K. D. Hahn, M. S. Rubery, O. L. Landen, J. D. Moody, L. Aghaian, A. Allen, S. H. Baxamusa, S. D. Bhandarkar, J. Biener, N. W. Birge, T. Braun, T. M. Briggs, C. Choate, D. S. Clark, J. W. Crippen, C. Danly, T. Döppner, M. Durocher, M. Erickson, T. Fehrenbach, M. Freeman, M. Havre, S. Hayes, T. Hilsabeck, J. P. Holder, K. D. Humbird, O. A. Hurricane, N. Izumi, S. M. Kerr, S. F. Khan, Y. H. Kim, C. Kong, J. Jeet, B. Kozioziemski, A. L. Kritcher, K. M. Lamb, N. C. Lemos, B. J. Macgowan, A. J. Mackinnon, A. G. Macphee, E. V. Marley, K. Meaney, M. Millot, J. M. D. Nicola, A. Nikroo, R. Nora, M. Ratledge, J. S. Ross, S. J. Shin, V. A. Smalyuk, M. Stadermann, S. Stoupin, T. Suratwala, C. Trosseille, B. V. Wonterghem, C. R. Weber, C. Wild, C. Wilde, P. T. Wooddy, B. N. Woodworth, and C. V. Young, "Observations and properties of the first laboratory fusion experiment to exceed a target gain of unity," Phys. Rev. E **109**, 025203 (2024).

[4]O. A. Hurricane, D. A. Callahan, D. T. Casey, A. R. Christopherson, A. L. Kritcher, O. L. Landen, S. A. Maclaren, R. Nora, P. K. Patel, J. Ralph, D. Schlossberg, P. T. Springer, C. V. Young, and A. B. Zylstra, "Energy principles of scientific breakeven in an inertial fusion experiment," Phys. Rev. Lett. **132**, 065103 (2024).

[5]A. L. Kritcher, A. B. Zylstra, C. R. Weber, O. A. Hurricane, D. A. Callahan, D. S. Clark, L. Divol, D. E. Hinkel, K. Humbird, O. Jones, J. D. Lindl, S. Maclaren, D. J. Strozzi, C. V. Young, A. Allen, B. Bachmann, K. L. Baker, T. Braun, G. Brunton, D. T. Casey, T. Chapman, C. Choate, E. Dewald, J. M. D. Nicola, M. J. Edwards, S. Haan, T. Fehrenbach, M. Hohenberger, E. Kur, B. Kustowski, C. Kong, O. L. Landen, D. Larson, B. J. Macgowan, M. Marinak, M. Millot, A. Nikroo, R. Nora, A. Pak, P. K. Patel, J. E. Ralph, M. Ratledge, M. S. Rubery, D. J. Schlossberg, S. M. Sepke, M. Stadermann, T. I. Suratwala, R. Tommasini, R. Town, B. Woodworth, B. V. Wonterghem, and C. Wild, "Design of the first fusion experiment to achieve target energy gain $g > 1$," Phys. Rev. E **109**, 025204 (2024).

[6]H. Abu-Shawareb *et al.*, "Achievement of target gain larger than unity in an inertial fusion experiment," Phys. Rev. Lett. **132**, 065102 (2024).

[7]W. Trickey, V. N. Goncharov, R. Betti, E. M. Campbell, T. J. Collins, and R. K. Follett, "The physics of gain relevant to inertial fusion energy target designs," Phys. Plasmas **31**, 12702 (2024).

[8]D. S. Hodge, A. F. T. Leong, S. Pandolfi, K. Kurzer-Ogul, D. S. Montgomery, H. Aluie, H. Aluie, C. Bolme, T. Carver, E. Cunningham, C. B. Curry, C. B. Curry, M. Dayton, F.-J. Decker, E. Galtier, P. Hart, D. Khaghani, H. J. Lee, K. Li, Y. Liu, K. Ramos, J. Shang, J. Shang, S. Vetter, B. Nagler, R. L. Sandberg, and A. E. Gleason, "Multi-frame, ultrafast, x-ray microscope for imaging shockwave dynamics," Opt. Express **30**(21), 38405–38422 (2022).

[9]J. Biener, C. Dawedeit, S. H. Kim, T. Braun, M. A. Worsley, A. A. Chernov, C. C. Walton, T. M. Willey, S. O. Kucheyev, S. J. Shin, Y. M. Wang, M. M. Biener, J. R. Lee, B. J. Kozioziemski, T. V. Buuren, K. J. Wu, J. H. Satcher, and A. V. Hamza, "A new approach to foam-lined indirect-drive NIF ignition targets," Nucl. Fusion **52**, 062001 (2012).

[10]Z. Lin, T. Yongjian, Z. Chifeng, L. Xuan, and Z. Houqiong, "Preparation and characterization of deuterated polymer foams for thermal nuclear fusion targets," Nucl. Instrum. Methods Phys. Res., Sect. A **480**, 242–245 (2002).

[11]S. K. Saha, "Additively manufactured nanoporous foam targets for economically viable inertial fusion energy," Soc. Impacts **3**, 100029 (2024).

[12]R. A. Sacks and D. H. Darling, "Direct drive cryogenic ICF capsules employing d-t wetted foam," Nucl. Fusion **27**, 447 (1987).

[13]R. E. Olson, M. J. Schmitt, B. M. Haines, G. E. Kemp, C. B. Yeamans, B. E. Blue, D. W. Schmidt, A. Haid, M. Farrell, P. A. Bradley, H. F. Robey, and R. J. Leeper, "A polar direct drive liquid deuterium-tritium wetted foam target concept for inertial confinement fusion," Phys. Plasmas **28**, 122704 (2021).

[14]T. Cardenas, T. J. Murphy, L. Kuettner, B. Patterson, L. Goodwin, K. Cluff, J. Oertel, T. Day, S. Edwards, C. E. Hamilton, R. Randolph, K. Henderson, J. Cowan, S. J. Shin, S. Bhandarkar, and B. J. Kozioziemski, "Material characterization of hierarchical tunable pore size polymer foams used in the marble mix morphology experiment," Fusion Sci. Technol. **76**, 795–806 (2020).

[15]K. S. Lee, D. Y. Yang, S. H. Park, and R. H. Kim, "Recent developments in the use of two-photon polymerization in precise 2d and 3d microfabrications," Polym. Adv. Technol. **17**, 72–82 (2006).

[16]X. Zhou, Y. Hou, and J. Lin, "A review on the processing accuracy of two-photon polymerization," AIP Adv. **5**, 30701 (2015).

[17]A. Ostendorf and B. N. Chichkov, "Two-photon polymerization: A new approach to micromachining," Photonics Spectra **40**, 72 (2006).

[18]U. Kleuker, "X-ray diffraction computed tomography: A survey and description," in *Developments in X-Ray Tomography* (SPIE, 1997), Vol. 3149, pp. 245–256.

[19]M. Dierolf, A. Menzel, P. Thibault, P. Schneider, C. M. Kewish, R. Wepf, O. Bunk, and F. Pfeiffer, "Ptychographic x-ray computed tomography at the nanoscale," Nature **467**, 436–439 (2010).

[20]M. Holler, A. Diaz, M. Guizar-Sicairos, P. Karvinen, E. Färm, E. Härkönen, M. Ritala, A. Menzel, J. Raabe, and O. Bunk, "X-ray ptychographic computed tomography at 16 nm isotropic 3d resolution," Sci. Rep. **4**, 3857 (2014).

[21]F. Pfeiffer, "X-ray ptychography," Nat. Photonics **12**(1), 9–17 (2018).

[22]A. Carr, Y. Sechrest, K. Mertes, B. M. Patterson, B. Wohlberg, L. Hancock, N. Sirica, R. Sandberg, C. Sweeney, J. Hunter *et al.*, "Morphology of copper nanofoams for radiation hydrodynamics and fusion applications investigated by 3d ptychotomography," Nano Lett. **24**, 9916–9922 (2024).

[23]B. A. Pound, K. M. Mertes, A. V. Carr, M. H. Seaberg, M. S. Hunter, W. C. Ward, J. F. Hunter, C. M. Sweeney, C. M. Sewell, N. R. Weisse-Bernstein *et al.*, "Ptychography at the linac coherent light source in a parasitic geometry," J. Appl. Crystallogr. **53**, 1276–1282 (2020).

[24]A. Mozzanica, M. Andrä, R. Barten, A. Bergamaschi, S. Chiriotti, M. Brückner, R. Dinapoli, E. Fröjdh, D. Greiffenberg, F. Leonarski *et al.*, "The Jungfrau detector for applications at synchrotron light sources and XFELS," Synchrotron Radiat. News **31**, 16–20 (2018).

[25]M. Endrizzi, "X-ray phase-contrast imaging," Nucl. Instrum. Methods Phys. Res., Sect. A **878**, 88–98 (2018).

[26]C. Sweeney, K. Mertes, A. Carr, Y. Sechrest, N. Sirica, A. Gleason, R. Sandberg, and N. Weisse-Bernstein, "Interfacility data processing workflow for real-time imaging," in *Poster Presented at Conference on Data Analysis (CoDA), Santa Fe, New Mexico, USA* (LANL, 2023).

[27]M. Zemek, J. Šalplachta, T. Zikmund, K. Omote, Y. Takeda, P. Oberta, and J. Kaiser, "Automatic marker-free estimation methods for the axis of rotation in sub-micron x-ray computed tomography," Tomography Mater. Struct. **1**, 100002 (2023).

[28]D. Gürsoy, Y. P. Hong, K. He, K. Hujsak, S. Yoo, S. Chen, Y. Li, M. Ge, L. M. Miller, Y. S. Chu, V. D. Andrade, K. He, O. Cossairt, A. K. Katsaggelos, and C. Jacobsen, "Rapid alignment of nanotomography data using joint iterative reconstruction and reprojection," Sci. Rep. **7**, 12141 (2017).

[29]M. Odstrčil, M. Holler, J. Raabe, and M. Guizar-Sicairos, "Alignment methods for nanotomography with deep subpixel accuracy," Opt. Express **27**, 36637 (2019).

[30]C. Zach, T. Pock, and H. Bischof, "A duality based approach for realtime tv-l 1 optical flow," in *Pattern Recognition: 29th DAGM Symposium, Heidelberg, Germany, September 12–14, 2007* (Springer, 2007), pp. 214–223.

[31]J. Schindelin, I. Arganda-Carreras, E. Frise, V. Kaynig, M. Longair, T. Pietzsch, S. Preibisch, C. Rueden, S. Saalfeld, B. Schmid, J. Y. Tinevez, D. J. White, V. Hartenstein, K. Eliceiri, P. Tomancak, and A. Cardona, "Fiji: An open-source platform for biological-image analysis," Nat. Methods **9**, 676–682 (2012).

[32]N. T. Vo, M. Drakopoulos, C. Reinhard, and R. C. Atwood, "Reliable method for calculating the center of rotation in parallel-beam tomography," Opt. Express **22**(16), 19078–19086 (2014).

14 October 2025 21:21:13

© Author(s) 2025

[33]D. Gürsoy, F. De Carlo, X. Xiao, and C. Jacobsen, "Tomopy: A framework for the analysis of synchrotron tomographic data," J. Synchrotron Rad. **21**, 1188–1193 (2014).
[34]D. M. Pelt, D. Gürsoy, W. J. Palenstijn, J. Sijbers, F. D. Carlo, and K. J. Batenburg, "Integration of tomopy and the astra toolbox for advanced processing and reconstruction of tomographic synchrotron data," J. Synchrotron Rad. **23**, 842–849 (2016).
[35]S. D. Team, see https://github.com/cabouman/svmbir for "Super-voxel model based iterative reconstruction (SVMBIR)," (Software Library, 2024).
[36]K. Giewekemeyera, P. Thibault, S. Kalbfleisch, A. Beerlink, C. M. Kewish, M. Dierolf, F. Pfeiffer, and T. Salditta, "Quantitative biological imaging by ptychographic x-ray diffraction microscopy," Proc. Natl. Acad. Sci. U. S. A. **107**, 529–534 (2010).
[37]S. Koho, G. Tortarolo, M. Castello, T. Deguchi, A. Diaspro, and G. Vicidomini, "Fourier ring correlation simplifies image restoration in fluorescence microscopy," Nat. Commun. **10**, 11024 (2019).
[38]B. Rieger, B. Rieger, I. Droste, F. Gerritsma, T. Ten Brink, S. Stallinga, and S. Stallinga, "Single image Fourier ring correlation," Opt. Express **32**(12), 21767–21782 (2024).
[39]M. V. Heel and M. Schatz, "Fourier shell correlation threshold criteria," J. Struct. Biol. **151**, 250–262 (2005).
[40]P. Sidorenko and O. Cohen, "Single-shot ptychography," Optica **3**(1), 9–14 (2016).
[41]T. J. Davis, D. Gao, T. E. Gureyev, A. W. Stevenson, and S. W. Wilkins, "Phase-contrast imaging of weakly absorbing materials using hard x-rays," Nature **373**(6515), 595–598 (1995).

14 October 2025 21:21:13

© Author(s) 2025